

Vector magnetometry in zero bias magnetic field using nitrogen-vacancy ensembles

Chunxing Li(李春兴), Fa-Zhan Shi(石发展), Jingwei Zhou(周经纬), and Peng-Fei Wang(王鹏飞)

Citation: Chin. Phys. B, 2024, 33 (**10**): 100701. DOI: 10.1088/1674-1056/ad73af
Journal homepage: http://cpb.iphy.ac.cn; http://iopscience.iop.org/cpb

What follows is a list of articles you may be interested in

Performance optimization of a SERF atomic magnetometer based on flat-top light beam

Ziqi Yuan(袁子琪), Junjian Tang(唐钧剑), Shudong Lin(林树东), and Yueyang Zhai(翟跃阳)
Chin. Phys. B, 2024, 33 (**6**): 060703. DOI: 10.1088/1674-1056/ad401b

Response optimization of a three-axis sensitive SERF magnetometer for closed-loop operation

Yuanrui Zhou(周原锐), Yongze Sun(孙永泽), Xixi Wang(汪茜茜), Jianan Qin(秦佳男), Xue Zhang(张雪), and Yanzhang Wang(王言章)
Chin. Phys. B, 2024, 33 (**2**): 020701. DOI: 10.1088/1674-1056/ad0b00

Current sensor based on diamond nitrogen-vacancy color center

Zi-Yang Shi(史子阳), Wei Gao(高伟), Qi Wang(王启), Hao Guo(郭浩), Jun Tang(唐军), Zhong-Hao Li(李中豪), Huan-Fei Wen(温焕飞), Zong-Min Ma(马宗敏), and Jun Liu(刘俊)
Chin. Phys. B, 2023, 32 (**7**): 070704. DOI: 10.1088/1674-1056/acc3fe

Asymmetric magnetoimpedance effect and dipolar interactions of FINEMET/SiO_2/FePd composite ribbons

Yong-Bin Guo(郭永斌), Dao Wang(王岛), Zhong-Min Wang(王忠民), Lei Ma(马垒), and Zhen-Jie Zhao(赵振杰)
Chin. Phys. B, 2023, 32 (**7**): 070703. DOI: 10.1088/1674-1056/acad6e

A robust method for performance evaluation of the vapor cell for magnetometry

Zhi Liu(柳治), Sheng Zou(邹升), Kaifeng Yin(尹凯峰), Tao Shi(石韬),Junjian Tang(唐钧剑), and Heng Yuan(袁珩)
Chin. Phys. B, 2023, 32 (**4**): 040703. DOI: 10.1088/1674-1056/aca6d5

SPECIAL TOPIC — Quantum computing and quantum sensing

Vector magnetometry in zero bias magnetic field using nitrogen-vacancy ensembles

Chunxing Li(李春兴)[1,2], Fa-Zhan Shi(石发展)[1,2,3], Jingwei Zhou(周经纬)[1,2,3], and Peng-Fei Wang(王鹏飞)[1,2,3,†]

[1] *CAS Key Laboratory of Microscale Magnetic Resonance and School of Physical Sciences, University of Science and Technology of China, Hefei* 230026, *China*

[2] *CAS Center for Excellence in Quantum Information and Quantum Physics, University of Science and Technology of China, Hefei* 230026, *China*

[3] *Hefei National Laboratory, University of Science and Technology of China, Hefei* 230088, *China*

(Received 30 April 2024; revised manuscript received 25 August 2024; accepted manuscript online 27 August 2024)

The application of the vector magnetometry based on nitrogen-vacancy (NV) ensembles has been widely investigated in multiple areas. It has the superiority of high sensitivity and high stability in ambient conditions with microscale spatial resolution. However, a bias magnetic field is necessary to fully separate the resonance lines of optically detected magnetic resonance (ODMR) spectrum of NV ensembles. This brings disturbances in samples being detected and limits the range of application. Here, we demonstrate a method of vector magnetometry in zero bias magnetic field using NV ensembles. By utilizing the anisotropy property of fluorescence excited from NV centers, we analyzed the ODMR spectrum of NV ensembles under various polarized angles of excitation laser in zero bias magnetic field with a quantitative numerical model and reconstructed the magnetic field vector. The minimum magnetic field modulus that can be resolved accurately is down to ~ 0.64 G theoretically depending on the ODMR spectral line width (1.8 MHz), and ~ 2 G experimentally due to noises in fluorescence signals and errors in calibration. By using ^{13}C purified and low nitrogen concentration diamond combined with improving calibration of unknown parameters, the ODMR spectral line width can be further decreased below 0.5 MHz, corresponding to ~ 0.18 G minimum resolvable magnetic field modulus.

Keywords: vector magnetometry, NV ensembles, optically detected magnetic resonance (ODMR), zero bias magnetic field

PACS: 07.55.Ge, 07.57.Pt, 76.70.Hb, 76.30.Mi **DOI:** 10.1088/1674-1056/ad73af

1. Introduction

Nitrogen-vacancy (NV) centers in diamond are versatile and atomic sized quantum sensors. The ground state of the electron spin ($S = 1$) of negatively charged NV center can be initialized and readout using optical method.[1] The sublevel states $m_s = 0$ and $m_s = \pm 1$ in the ground state of NV center can be controlled using microwave field (Fig. 1(b)). The long decoherence time of NV center in room temperature makes it a sensitive sensor[2–4] for sensing magnetic field,[5–7] electric field,[8,9] temperature,[10,11] or stress.[12,13] Magnetometry based on NV ensembles in diamond has been widely applied in research of magnetic functional materials,[14,15] rock magnetization,[16,17] chip inspection[18] and geophysics.[19] It has advantages of high sensitivity, microscale spatial resolution, and full vector magnetic field sensing capacity.[5]

The experimental method to realize magnetometry using NV centers is optically detected magnetic resonance (ODMR). There are four different crystallographic orientations of NV centers in diamond (Fig. 1(a)). In order to reconstruct the magnetic field vector, the Zeeman splitting of all the four kinds of NV centers NV$_i$ ($i = 1, 2, 3, 4$) needs to be extracted from ODMR spectrum of NV ensembles[6] (Fig. 1(c)). The sensitivity of this method can achieve nanoTesla per square Hertz and the minimum detectable magnetic field variation is up to sub-nanoTesla. However, these values are achieved under a bias field. When the bias field is absent and the concerned magnetic field of sample is weak, the ODMR spectral lines of all the four orientations of NV centers become highly overlapped and hard to distinguish (Fig. 1(d)). A common fitting method to reconstruct the magnetic field $\boldsymbol{B}$ sensed by NV centers is invalid in this circumstance. In another situation, when the magnetic field is along some specific directions, for example one of the three axes of the system in Fig. 1(a), even the modulus of $\boldsymbol{B}$ is big enough, the ODMR spectra are still overlapped or partially overlapped. The reconstruction of $\boldsymbol{B}$ is also invalid in this situation with no prior knowledge about the direction of $\boldsymbol{B}$, which is often true for an ordinary magnetic sample (supplementary Fig. S1).

The concerned magnetic field $\boldsymbol{B}$ is obtained by subtracting the bias field $\boldsymbol{B}_0$ from the measured magnetic field result $\boldsymbol{B}_{\rm tot}$. The bias field $\boldsymbol{B}_0$ (usually $|\boldsymbol{B}_0| > 20$ G) may bring some negative influences to the magnetization of the samples being measured. For example, ferromagnetic grains accumulate viscous remanent magnetization (VRM) in environment magnetic field during a period of time. In rock magnetism research, to protect the original remanent magnetization infor-

†Corresponding author. E-mail: wpf@ustc.edu.cn

© 2024 Chinese Physical Society and IOP Publishing Ltd

mation of ferromagnetic grains wrapped in rocks from being disturbed by VRM, the rock samples must stay in magnetic shield environment.[20] In another situation, a bias field may disturb the observation of dynamic process of a target being researched in magnetic film materials, such as spin waves and magnetic skyrmions. On the other hand, the deviations of $\boldsymbol{B}_0$ could also bring extra error.

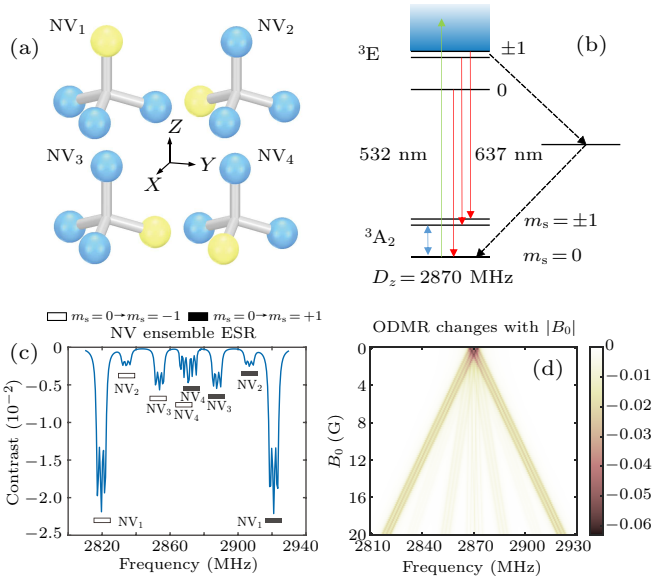


Fig. 1. ODMR spectrum of NV ensembles. (a) Four crystallographic orientations of NV in diamond. (b) Energy levels of NV electron spin. (c) Optically detected magnetic resonance (ODMR) spectrum of NV ensembles simulated in conditions where all eight groups of spectral lines are divided. The magnetic field sensed by NV ensembles is set as $\boldsymbol{B}_0 = (B_0, \theta, \alpha) = (20\ \text{G}, 25^\circ 30^\circ)$. The spectral lines are labeled by the corresponding crystallographic orientation of NV, as shown in (a). (d) Simulated ODMR spectrum when B_0 changes from 20 G to 0 G. The spectral lines of ODMR spectrum become highly overlapped as B_0 becomes smaller, which makes it hard to distinguish the corresponding orientation of NV centers.

There has been some reported NV magnetometry with no bias field. Till Lenz *et al.*[21] made use of the selective excitation of a single NV center with a circularly polarized microwave radiation circuit. This effectively avoids nonlinear relations of NV energy levels and the sensed magnetic field modulus in zero to near-zero field due to level anticrossing in states with the same I_z. However, only axial magnetic component B_z is measurable. Huijie Zheng *et al.*[22] used the same method of selective excitation of NV ensembles with circularly polarized microwave field. They also combined a modulation-demodulation system to resolve the magnetic field modulus in ultralow field with a bandwidth within ± 1 μT. But this still can only extract axial magnetic component. Münzhuber *et al.*[23] utilized polarization selective laser excitation to assign all the distinct resonance peaks to their corresponding orientations of NV centers. This method resolves the complexity of ODMR spectra of NV ensembles when all the resonance peaks are separable without overlaps and has the capacity of vector reconstruction. However, the minimum value of the modulus of measurable magnetic field is larger than 20 G, otherwise the spectral lines will overlap and become indistinguishable.

In this paper, to solve the problem that the $4 \times 6 = 24$ ODMR spectral lines of NV ensembles are overlapped in zero bias magnetic field, which makes the reconstruction of $\boldsymbol{B}$ infeasible, we established an accurate numerical model to quantitatively describe the ODMR spectrum of NV ensembles under various polarizing angles θ_e of the input linearly polarized laser. By rotating θ_e from 0 to π and measuring the ODMR spectrum at every point of θ_e, a normalized two-dimensional fluorescence spectrum $P_{\text{norm}}(\omega, \theta_e)$ is obtained, where ω is the microwave frequency. The anisotropic fluorescence intensities of four orientations of NV centers as a function of θ_e leave different characteristic features in this two-dimensional fluorescence spectrum, even the ODMR spectral lines are overlapped. So the concerned magnetic field vector $\boldsymbol{B}$ can be fitted from measured $P_{\text{norm}}(\omega, \theta_e)$ pattern by a two-dimensional nonlinear least-square algorithm using our numerical model.

The challenge lies in the numerical model with many unknown parameters needed to be determined. To ensure the agreement of those parameters with the actual experiment conditions, the whole system was carefully calibrated first. The calculated $P_{\text{norm}}(\omega, \theta_e)$ pattern with fitting results is very close to the experiment data, and the relative error of reconstructed magnetic field vector is at most 9.7%. This vector magnetometry method in zero bias magnetic field has high measurement dynamic range. The minimum modulus of measurable magnetic field vector $|\boldsymbol{B}_{\text{min}}|$ is down to 2 G in experiment due to noises in fluorescence signal and measurement uncertainties of calibrated parameters. $|\boldsymbol{B}_{\text{min}}|$ can be further decreased to ~ 0.64 G with a more precise calibration.

2. Experiment setup and control circuits

The experiment setup and pulse sequences are shown in Fig. 2. This is a typical wide-field ODMR experiment platform for NV ensembles. A 532 nm laser is used to excite and readout the electron spin state of NV centers. Two acoustic optical modulators (AOMs) are used to control the laser sequence and generate laser pulses. The light beam is expanded by an expander to generate a large field of view (200 μm×200 μm at most). A polarized beam splitter (PBS) is used to eliminate s-polarized component of input laser and select p-polarized component. A half-wave plate mounted on a motorized rotation stage is used to control the polarized angle θ_e of the laser beam projected on NV centers. A long pass dichroic mirror is used to separate input 532 nm exciting laser beam and output collecting fluorescence light path ($>$ 630 nm). A sCMOS camera is used to readout the NV fluorescence collected by an Olympus LUCPLFLN 40× objective. A set of three-dimensional Helmholtz coils is used to cancel background magnetic field (mostly the Earth's magnetic field) and generate a static magnetic field $\boldsymbol{B} = \boldsymbol{B}_0\ (\sin\theta\cos\alpha, \sin\theta\sin\alpha, \cos\theta)$ to simulate the field of a magnetic sample to be measured.

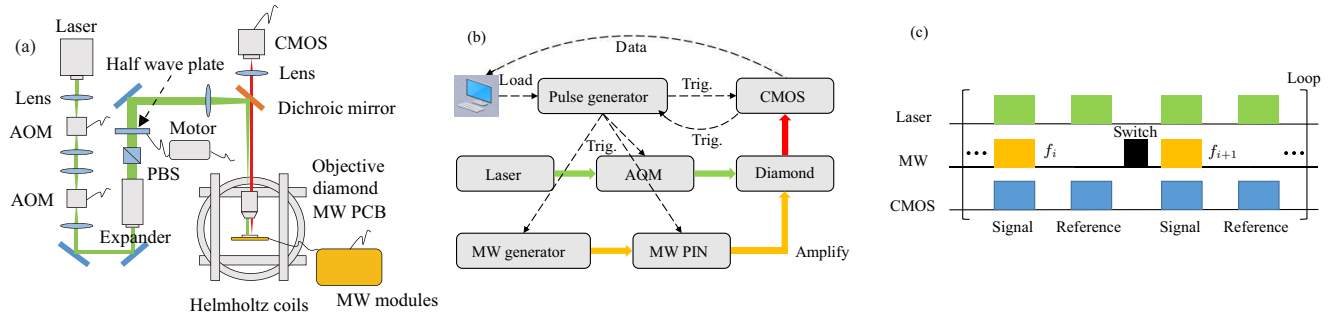


Fig. 2. Experiment setup. (a) Sketch of the experiment setup. (b) The full-hardware-control electronic circuits. (c) Continuous wave sequences of ODMR.

A 1.2 mm×1.2 mm×0.6 mm sized diamond sample with low electric/strain field cut from a {100} CVD diamond plate (Element Six) with [N] ∼ 1 ppm is used and placed on the central region of a coplanar waveguide. With limited accuracy of mechanical cutting craft, the crystal angle of the cut diamond has a mismatch from the desirable {111} direction. The coplanar waveguide fabricated on a printed circuit board (PCB) is used to transmit and radiate the microwave field generated by a RIGOL DSG3060 radio frequency (RF) source to control the electron spin state of NV centers. This waveguide is designed to radiate microwave field parallel to the surface of PCB and has a broadband working range from 0.35 kHz to 6 GHz. The radiation efficiency is upper than 90% within this working frequency range.

The control circuits of the instrument are shown in Fig. 2(b). A pulse generator (PulseBlaster, PB) is used to control the pulse sequences via TTL signals to finish all the time ordered operations of the laser, microwave, and sCMOS (scientific Complementary Metal Oxide Semiconductor) camera. In these circuits, a PIN switch is used to switch the on-off state of microwave (MW) to general MW pulses. PB also triggers AOM to control the laser pulses, and initializes the starting of the exposure operation of the sCMOS camera. To guarantee the success of every exposure operation of the camera and also save the sequence's execution time, a feedback line is linked from the sCMOS camera to the PB (see Fig. 2(b)). A TTL pulse is generated by the camera transmitted in this line after an exposure operation is finished. This TTL signal triggers PB to output the next pulse operations just after a picture has been taken by the camera and stored in the computer. This feedback process minimizes unwanted communication time between two exposures. During the whole experiment, after the pulse sequences are loaded into the memory of PB, the remaining control of the instrument is all done by PB in a "hardware way". This full hardware control mode vastly increases the utilization efficiency of picture exposure time.

The pulse sequences loaded into PB are shown in Fig. 2(c). This is a typical continuous wave sequence of ODMR.[24] The final fluorescence contrast signal shown in ODMR spectra is defined as contrast = (signal − reference)/reference. After taking the fluorescence picture of signal and reference on one microwave frequency f_i, PB then triggers the MW source to switch onto the next frequency f_{i+1}. The signal and reference fluorescence are recorded on every frequency point, and this frequency sweeping process is repeated for several loops in order to improve the signal-to-noise ratio.

3. The numerical model of the two-dimensional ODMR spectrum

The system of the numerical model of the two-dimensional ODMR spectrum $P_{\rm norm}(\omega, \theta_{\rm e})$ is shown in Fig. 3. The laser beam was set to be not along the $-Z$ axis. To describe both the deviations of the [111] direction of cut diamond and the laser beam from Z axis, four rotational angles β_1, φ_1, β_2, φ_2 are introduced.

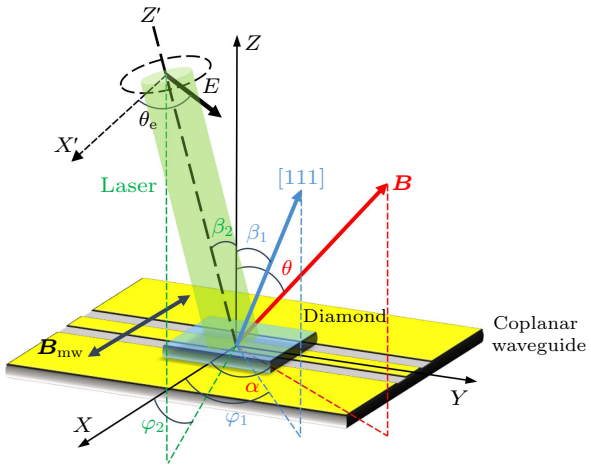


Fig. 3. The $P_{\rm norm}(\omega, \theta_{\rm e})$ pattern numerical model. A near {111} facet cut diamond containing NV ensembles is set on a coplanar waveguide which transmits linearly polarized microwave field $\boldsymbol{B}_{\rm mw}$ along x axis to control the NV electron spin state. A linearly polarized 532 nm laser irradiates the diamond to excite and read out the NV electron spin state. The [111] crystallographic direction of the diamond and the laser beam have deviations from Z-axis direction.

The rotation transformation matrix to describe the deviation of the [111] direction of diamond is $\boldsymbol{R}_1(\beta_1, \varphi_1) = \boldsymbol{R}_z(\varphi_1) \cdot \boldsymbol{R}_y(\beta_1)$, where $\boldsymbol{R}_y(\beta_1)$ and $\boldsymbol{R}_z(\varphi_1)$ are the rotation transformation matrices along y-axis by β_1 and along z-axis

by φ_1, respectively,

$$\boldsymbol{R}_y(\beta_1)=\begin{pmatrix}\cos\beta_1 & 0 & \sin\beta_1\\ 0 & 1 & 0\\ -\sin\beta_1 & 0 & \cos\beta_1\end{pmatrix}, \tag{1}$$

$$\boldsymbol{R}_z(\varphi_1)=\begin{pmatrix}\cos\varphi_1 & -\sin\varphi_1 & 0\\ \sin\varphi_1 & \cos\varphi_1 & 0\\ 0 & 0 & 1\end{pmatrix}. \tag{2}$$

The actual direction vectors of the quantum axis of NV$_i$ ($i=1$, 2, 3, 4) are

$$\boldsymbol{n}_i'=\boldsymbol{R}_1(\beta_1,\varphi_1)\cdot\boldsymbol{n}_i, \tag{3}$$

where $\boldsymbol{n}_i$ are the ideal direction vectors of NV$_i$

$$\begin{aligned}&\boldsymbol{n}_1=(0,0,1),\quad \boldsymbol{n}_2=\frac{\left(-\sqrt{2},-\sqrt{6},-1\right)}{3},\\ &\boldsymbol{n}_3=\frac{\left(-\sqrt{2},\sqrt{6},-1\right)}{3},\quad \boldsymbol{n}_4=\frac{\left(2\sqrt{2},0,-1\right)}{3}.\end{aligned} \tag{4}$$

The rotation transformation matrix to describe the deviation of the laser beam is $\boldsymbol{R}_2(\beta_2,\varphi_2)=\boldsymbol{R}_z(\varphi_2)\cdot\boldsymbol{R}_y(\beta_2)$, which has the same form as $\boldsymbol{R}_1(\beta_1,\varphi_1)$. The actual electric field vector of input laser beam $\boldsymbol{E}_l'$ is expressed as

$$\boldsymbol{E}_l'=\boldsymbol{R}_2(\beta_2,\varphi_2)\cdot\boldsymbol{E}_l, \tag{5}$$

$$\boldsymbol{E}_l=E_{\rm m}(\cos\theta_{\rm e},\sin\theta_{\rm e},0). \tag{6}$$

To express $P_{\rm norm}(\omega,\theta_{\rm e})$ pattern explicitly, the central frequencies, the shape of ODMR spectrum lines, and the anisotropic features of the fluorescence contrast when the polarized angle of the laser beam is changed are analyzed quantitatively in the following.

First, we calculate the eigenvalues of Hamiltonian of NV ensembles to get the resonant frequencies of four different orientations of NV centers. The Hamiltonian of NV$_i$ ($i=1$, 2, 3, 4) is[21]

$$\begin{aligned}\frac{H_i}{h}&=(D_z+E_z)S_z^2+E_x\left(S_y^2-S_x^2\right)\\ &\quad+E_y(S_xS_y+S_yS_x)+\gamma\boldsymbol{B}\cdot\boldsymbol{S}+\boldsymbol{S}\cdot\overleftrightarrow{A}\cdot\boldsymbol{I}\\ &\approx(D_z+E_z)S_z^2+E_x\left(S_y^2-S_x^2\right)+E_y(S_xS_y+S_yS_x)\\ &\quad+\gamma B_{i\|}S_z+A_{zz}S_z\cdot I_z.\end{aligned} \tag{7}$$

Here $D_z=2870$ MHz is the zero-field splitting of NV center. E_x, E_y and E_z are the strain terms. $\boldsymbol{B}$ is the magnetic field sensed by NV centers. $\boldsymbol{S}$ and $\boldsymbol{I}$ are the spin operator of NV center and ^{14}N nuclear spin, respectively. γ is the gyromagnetic ratio of NV electron spins. The transverse magnetic field $B_{i\perp}$ exerted on NV$_i$ is omitted. We assume that E_x, E_y and E_z values are the same for all NV centers. The solution of the eigenvalues of H_i is as follows:

$$\omega_{i1}=D_z+E_z-\sqrt{E_\perp^2+\gamma^2B_{i\|}^2}, \tag{8}$$

$$\omega_{i2}=D_z+E_z+\sqrt{E_\perp^2+\gamma^2B_{i\|}^2}, \tag{9}$$

$$\omega_{i3}=D_z+E_z-\sqrt{E_\perp^2+A_{zz}^2-2A_{zz}\gamma B_{i\|}+\gamma^2B_{i\|}^2}, \tag{10}$$

$$\omega_{i4}=D_z+E_z+\sqrt{E_\perp^2+A_{zz}^2-2A_{zz}\gamma B_{i\|}+\gamma^2B_{i\|}^2}, \tag{11}$$

$$\omega_{i5}=D_z+E_z-\sqrt{E_\perp^2+A_{zz}^2+2A_{zz}\gamma B_{i\|}+\gamma^2B_{i\|}^2}, \tag{12}$$

$$\omega_{i6}=D_z+E_z+\sqrt{E_\perp^2+A_{zz}^2+2A_{zz}\gamma B_{i\|}+\gamma^2B_{i\|}^2}, \tag{13}$$

$$E_\perp^2=E_x^2+E_y^2, \tag{14}$$

$$B_{i\|}=\boldsymbol{B}\cdot\boldsymbol{n}_i'. \tag{15}$$

Second, we consider the anisotropic properties of the fluorescence of NV electric dipoles. Single NV center has two electric dipoles perpendicular to the quantum axis of NV center and also perpendicular to each other (Fig. 4(a)). The fluorescence intensity P_0 of a single NV center relates to the electric field of input laser $\boldsymbol{E}_l$ and the direction vector of the two electric dipoles $\boldsymbol{d}_1$ and $\boldsymbol{d}_2$ by[25]

$$P_0\propto c(|\boldsymbol{E}_l\cdot\boldsymbol{d}_1|^2+|\boldsymbol{E}_l\cdot\boldsymbol{d}_2|^2)=c\,|\boldsymbol{E}_l\times\boldsymbol{n}|^2, \tag{16}$$

where $\boldsymbol{n}$ is the direction vector parallel to the quantum axis of NV center. c is a proportional factor. Substituting $\boldsymbol{E}_l'=\boldsymbol{R}_2(\beta_2,\varphi_2)\cdot\boldsymbol{E}_l$ and $\boldsymbol{n}_i'=\boldsymbol{R}_1(\beta_1,\varphi_1)\cdot\boldsymbol{n}_i$ into Eq. (16), the normalized fluorescence intensity P_{0i} ($i=1$, 2, 3, 4) of single NV$_i$ in four different orientations changing with $\theta_{\rm e}$ can be calculated, $P_{0i}=c|(\boldsymbol{R}_2(\beta_2,\varphi_2)\cdot\boldsymbol{E}_l(\theta_{\rm e}))\times(\boldsymbol{R}_1(\beta_1,\varphi_1)\cdot\boldsymbol{n}_i)|^2$.

When β_1, φ_1, β_2, φ_2 equal 0 (i.e., there is no misalignment in the system), the calculation of P_{0i} is shown in Fig. 4(b). P_{0i} changes with $\theta_{\rm e}$ periodically and the extreme points of every P_{0i} are different, which makes the separable spectral lines distinguishable (Fig. 4(c)). From the experiment, we found the proportional factor c is not the same for different NV$_i$: $c_{2,3,4}=1$ and c_1 is 2–3.5. This happens because the fluorescence collection efficiency for NV$_1$ is larger than that for other three orientations of NV centers.[25]

To reconstruct the vector magnetic field, it is crucial to determine the resonant frequencies of four orientations of NV centers. When the sensed field of the concerned sample is weak in zero bias magnetic field, the spectral lines are overlapped and indistinguishable. But the effect of the anisotropic property of fluorescence still leaves characteristic features in the two-dimensional ODMR spectrum $P_{\rm norm}(\omega,\theta_{\rm e})$. From that, the magnetic field sensed by NV ensembles can be reconstructed.

Given the locations of all the energy sublevels ω_{ij} ($i=1$, 2, 3, 4; $j=1$, 2, 3, 4, 5, 6) and the normalized fluorescence intensities P_{0i} ($i=1$, 2, 3, 4), the fluorescence spectrum for single NV$_i$ can be modeled as[17]

$$P_i(\omega,\theta_{\rm e})=P_{0i}(\beta_1,\varphi_1,\beta_2,\varphi_2,c,\theta_{\rm e})$$

$$\times\left(1-\sum_{j=1}^{6}\frac{A_i\left(\frac{\Omega_i}{2}\right)^2}{(\omega-\omega_{ij}(\boldsymbol{B},\beta_1,\varphi_1))^2+\left(\frac{\Omega_i}{2}\right)^2}\right). \tag{17}$$

Here A_i is the fluorescence contrast of single NV$_i$. Ω_i is the spectral line width of NV$_i$. The shape of the ODMR spectral lines is modeled as Lorentzian. For diamond samples containing NV ensembles, supposing the proportion of four orientations of NV centers are 1:1:1:1, the total fluorescence contrast of NV ensembles is

$$\begin{aligned}P_{\rm norm}(\omega,\theta_{\rm e}) &= \frac{(P_1+P_2+P_3+P_4)-(P_{01}+P_{02}+P_{03}+P_{04})}{P_{01}+P_{02}+P_{03}+P_{04}}\\ &=\sum_{i=1}^{4}\frac{-P_{0i}(\beta_1,\varphi_1,\beta_2,\varphi_2,c,\theta_{\rm e})}{P_{01}+P_{02}+P_{03}+P_{04}}\\ &\quad\times\sum_{j=1}^{6}\frac{A_i(\frac{\Omega_i}{2})^2}{(\omega-\omega_{ij}(\boldsymbol{B},\beta_1,\varphi_1))^2+(\frac{\Omega_i}{2})^2},\end{aligned} \tag{18}$$

which builds a mapping between the sensed magnetic field $\boldsymbol{B}$ and the $P_{\rm norm}(\omega,\theta_{\rm e})$ pattern.

The symmetry of $P_{\rm norm}(\omega,\theta_{\rm e})$ is four-fold when β_1, φ_1, β_2, φ_2 are all zero. By doing this transformation of the sensed magnetic field $\boldsymbol{B}=(B_0,\theta,\alpha)$:

$$(\alpha\to\alpha+180^\circ)\vee(\theta\to180^\circ-\theta),$$

the same $P_{\rm norm}(\omega,\theta_{\rm e})$ is obtained for four different magnetic fields $\boldsymbol{B}=(B_0,\theta,\alpha)$. However, when $\beta_1,\beta_2\neq0$ and the laser beam is non-collinear with the [111] direction of the diamond, the symmetry of $P_{\rm norm}(\omega,\theta_{\rm e})$ decreases to two-fold.[27] Only a plus or minus sign is unsettled. The deviation of the laser beam from the direction of [111] crystal orientation of the diamond is necessary to gain an unambiguous reconstruction result. The ambiguity of the plus or minus sign can be further resolved by using a circularly polarized MW radiation structure.[23]

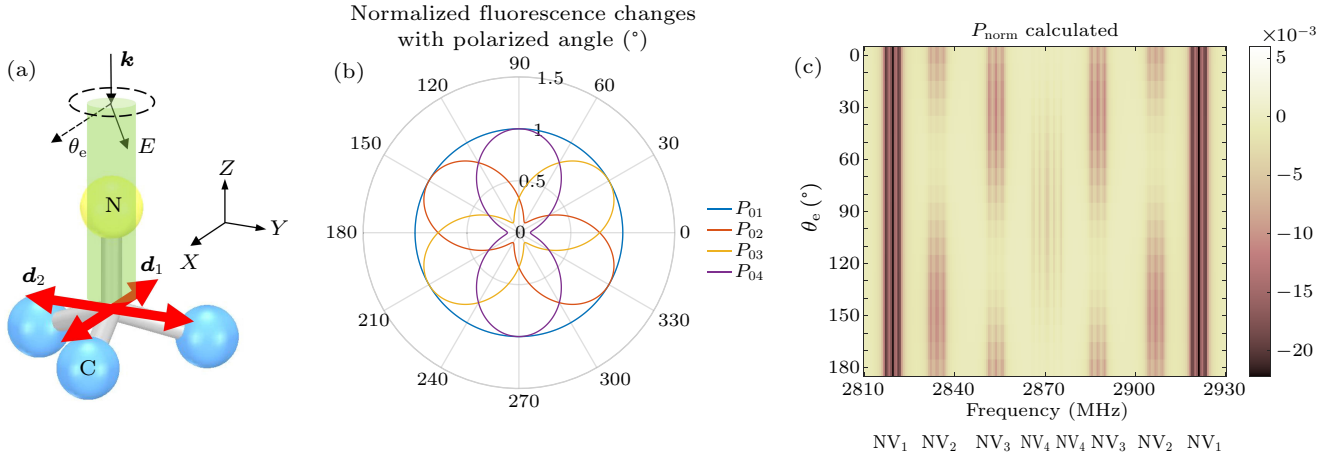


Fig. 4. Anisotropic properties of NV fluorescence (with no misalignment in the system). (a) Two transition dipoles of NV: $\boldsymbol{d}_1$ and $\boldsymbol{d}_2$. (b) Normalized fluorescence intensity P_{0i} ($i=1,2,3,4$) of single NV$_i$ in four different orientations changes with polarized angle $\theta_{\rm e}$ of the input 532 nm laser beam. (c) Simulated two-dimensional ODMR spectrum $P_{\rm norm}(\omega,\theta_{\rm e})$ in the same magnetic field as that in Fig. 1(c), $\boldsymbol{B}_0=(B_0,\theta,\alpha)=(20\ \text{G},25^\circ\ 30^\circ)$. The spectral lines are labeled by the corresponding orientations of NV centers.

4. Calibration

Before doing the measurement of $P_{\rm norm}(\omega,\theta_{\rm e})$ pattern and fitting the magnetic field, the environment magnetic field $\boldsymbol{B}_{\rm e}$ needs to be compensated and the magnetic shield environment needs to be ensured. We used a spectral method to measure the environment magnetic field. The details are in the supplementary.

After the magnetic shield environment is ensured, the unknown parameters of the numerical model of the near {111} facet cut diamond containing NV ensembles are calibrated. From Eqs. (1)–(18), the unknown parameters to be calibrated include

$$E_\perp,\ E_z,\ A_{zz},\ \Omega_i,\ \beta_1,\ \varphi_1,\ c,\beta_2,\ \varphi_2,\ A_i\quad(i=1,2,3,4).$$

The $E_\perp$, E_z, A_{zz}, Ω_i ($i=1,2,3,4$), β_1, φ_1 are directly measured by ODMR spectral method. c, β_2, φ_2, A_i ($i=1,2,3,4$) are fitted by Eq. (18) using a $P_{\rm norm}(\omega,\theta_{\rm e})$ experiment measured in a pre-set and known magnetic field $\boldsymbol{B}_{\rm c}$. All the measured ODMR spectra and two-dimensional ODMR spectra $P_{\rm norm}$ shown below are results averaged from the fluorescence signals collected in 3×3 pixels of the camera. This corresponds to a ~600 nm$\times600$ nm region in the diamond surface.

From Eqs. (8)–(15), when there is no magnetic field, all the energy eigenstates of four orientations of NV centers shown in ODMR spectrum are degenerated into four,

$$\omega_{01}=D_z+E_z-E_\perp, \tag{19}$$
$$\omega_{02}=D_z+E_z+E_\perp, \tag{20}$$
$$\omega_{03}=D_z+E_z-\sqrt{E_\perp^2+A_{zz}^2}, \tag{21}$$
$$\omega_{04}=D_z+E_z+\sqrt{E_\perp^2+A_{zz}^2}. \tag{22}$$

So a zero-field ODMR experiment is conducted to calibrate $E_\perp$, E_z, A_{zz} based on Eqs. (19)–(22). The central frequencies of the four spectral lines in zero field are fitted in this ODMR spectrum (Fig. 5(a)) and $E_\perp$, E_z, A_{zz} can be calculated from Eqs. (19)–(22). To measure the parameters Ω_i ($i = 1, 2, 3, 4$), β_1, φ_1, the spectral peaks of NV_i need to be fully divided and distinguished from each other. An ODMR experiment in a 20 G magnetic field $\boldsymbol{B}_\mathrm{c} = (B_0, \theta, \alpha) = (20\ \mathrm{G}, 135^\circ\ 150^\circ)$ was done for that (Fig. 5(b)). The width Ω_i of spectral lines of NV_i are directly fitted in this 20 G ODMR spectrum. Meanwhile, the central frequencies of all the eight groups of spectral lines ω_a ($a = 1, 2, \ldots, 8$) ordered from smallest to largest are also fitted out. The formula to fit this ODMR spectrum is

$$\begin{aligned} y = \sum_{a=1}^{8} \Bigg(& C_{3a-2} \frac{\Gamma_a^2}{4(\omega - \omega_a + A_{zz})^2 + \Gamma_a^2} \\ & + C_{3a-1} \frac{\Gamma_a^2}{4(\omega - \omega_a)^2 + \Gamma_a^2} \\ & + C_{3a} \frac{\Gamma_a^2}{4(\omega - \omega_a - A_{zz})^2 + \Gamma_a^2} \Bigg). \end{aligned} \tag{23}$$

In this equation, Γ_a ($a = 1, 2, \ldots, 8$) is the width of the spectral line whose central frequency corresponds to ω_a. It is supposed that $\Gamma_1 = \Gamma_8$, $\Gamma_2 = \Gamma_7$, $\Gamma_3 = \Gamma_6$, $\Gamma_4 = \Gamma_5$. The spectral lines of this ODMR spectrum can be distinguished as the magnetic field condition is already known (Fig. 5(b)). So it is determined that $\Gamma_1 = \Omega_3$, $\Gamma_2 = \Omega_4$, $\Gamma_3 = \Omega_1$, $\Gamma_4 = \Omega_2$.

After the eight frequencies ω_a are extracted, an optimization algorithm is utilized to calculate the rotational angles of [111] direction of the diamond β_1, φ_1. The objective function is

$$\begin{aligned} f_\mathrm{opt}(\beta_1, \varphi_1) = & (\omega_{31} - \omega_1)^2 + (\omega_{41} - \omega_2)^2 \\ & + (\omega_{11} - \omega_3)^2 + (\omega_{21} - \omega_4)^2 \\ & + (\omega_{22} - \omega_5)^2 + (\omega_{12} - \omega_6)^2 \\ & + (\omega_{42} - \omega_7)^2 + (\omega_{32} - \omega_8)^2. \end{aligned} \tag{24}$$

The ω_{ij} ($\boldsymbol{B}_\mathrm{c}$, β_1, φ_1) ($i = 1, 2, 3, 4$, $j = 1, 2$) are determined in Eqs. (8) and (9). ω_a ($a = 1, 2, \ldots, 8$) are fitted from the 20 G ODMR spectrum (Fig. 5(b)). Minimizing f_opt (β_1, φ_1) using simplex search method,[26] the values of the rotational angles of [111] direction β_1, φ_1 can be obtained.

For the other unknown parameters c, β_2, φ_2, A_i ($i = 1, 2, 3, 4$), it is hard to directly measure them accurately for NV ensembles. Fluorescence excited from one orientation of NV_i cannot be divided and selected out from total fluorescence of large NV ensembles, so the fluorescence imbalance parameter c is hard to measure. The rotation angles of the input laser beam β_2, φ_2 are hard to measure because of the short focal length of the object. And in Eq. (18), A_i couple with P_{0i}, which depend on more unknown parameters, and so they are hard to be determined directly.

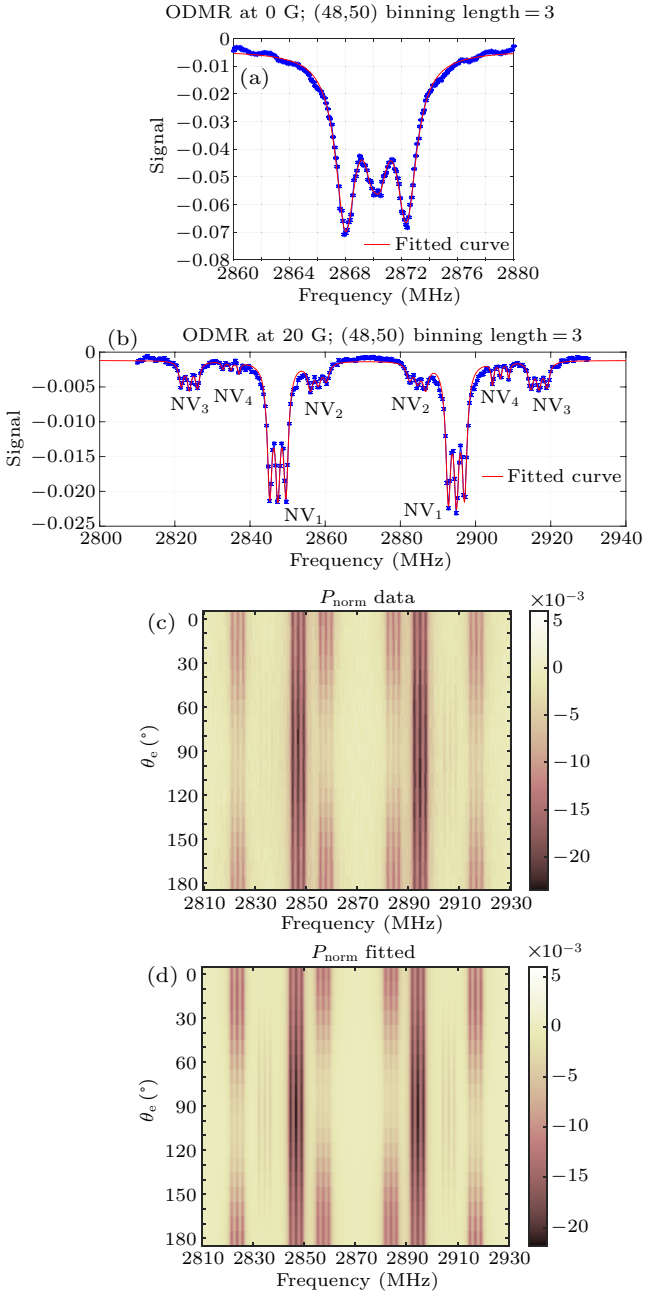


Fig. 5. Calibration of unknown parameters of the numerical model of $P_\mathrm{norm}(\omega, \theta_\mathrm{e})$. (a) ODMR spectrum of the NV ensembles measured at zero field. The locations of the spectral peaks are fitted to calculate three parameters $E_\perp$, E_z and A_{zz}. (b) A fully separated ODMR spectrum measured when the magnetic field is set as $\boldsymbol{B}_\mathrm{c} = (B_0, \theta, \alpha) = (20\ \mathrm{G}, 135^\circ, 150^\circ)$. The corresponding line widths Ω_i ($i = 1, 2, 3, 4$) and resonance frequencies ω_a ($a = 1, 2, \ldots, 8$) are fitted. An optimization method is used to determine the rotational angles (β_1 and φ_1) of [111] direction from ω_a ($a = 1, 2, \ldots, 8$). (c) The result of $P_\mathrm{norm}(\omega, \theta_\mathrm{e})$ measurement experiment at known magnetic field condition $\boldsymbol{B}_\mathrm{c} = (B_0, \theta, \alpha) = (20\ \mathrm{G}, 135^\circ, 150^\circ)$. (d) The fitting result of $P_\mathrm{norm}(\omega, \theta_\mathrm{e})$ pattern. Substituting fitted c, β_2, φ_2, A_i ($i = 1, 2, 3, 4$) into Eq. (18) combining with settled parameters $E_\perp$, E_z, A_{zz}, Ω_i ($i = 1, 2, 3, 4$), β_1, φ_1 and the magnetic field condition $\boldsymbol{B}_\mathrm{c}$ leads to this result.

These seven parameters, c, β_2, φ_2, A_i ($i = 1, 2, 3, 4$) can be classified into three kinds and each kind of them causes influence on the features of $P_\mathrm{norm}(\omega, \theta_\mathrm{e})$ spectrum independently (see supplementary for more details). So, a $P_\mathrm{norm}(\omega, \theta_\mathrm{e})$ measurement experiment (Fig. 5(c)) is carried out in known magnetic field $\boldsymbol{B}_\mathrm{c} = (B_0, \theta, \alpha) = (20\ \mathrm{G}, 135^\circ\ 150^\circ)$ to calibrate

these parameters. A multi-parameters nonlinear least-squares algorithm (trust-region method) is used to fit them with our numerical model, Eq. (18), from the experiment data shown in Fig. 5(c).

Table 1. Values of all the calibrated parameters. The measurement uncertainty of every parameter is determined by its 95% confidence interval given by the trust-region method. β_1 and φ_1 are given by optimization algorithm with no direct ways to assess their uncertainties.

Parameters	Values
$E_\perp$	0.3 ± 0.3 MHz
E_z	0.16 ± 0.03 MHz
A_{zz}	-2.16 ± 0.07 MHz
Ω_1	1.56 ± 0.04 MHz
Ω_2	1.8 ± 0.3 MHz
Ω_3	1.5 ± 0.2 MHz
Ω_4	0.8 ± 0.2 MHz
β_1	$-22.3°$
φ_1	$0.97°$
c	3.3 ± 0.8
β_2	$15° \pm 2°$
φ_2	$356° \pm 2°$
A_1	0.027 ± 0.003
A_2	0.042 ± 0.006
A_3	0.048 ± 0.007
A_4	0.019 ± 0.004

To avoid a local minimum rather than a global minimum of the fitting results appearing frequently in multi-parameters nonlinear least-square fitting based on optimization method, a selection strategy using random ergodic ideas is adopted and the best fitting group of all the unknown parameters is selected. The same selection strategy is also adopted in the fitting of the magnetic field vector in reconstruction. See the supplementary for more details about the selection strategy. The final fitting result in Fig. 5(d) agrees well with the experiment data.

Finally, all the unknown parameters of the numerical model are determined and listed in Table 1. These values of the parameters are used in the fitting program to reconstruct the magnetic field vector $\boldsymbol{B}$.

5. Reconstruction of magnetic vector in zero bias magnetic field using NV ensembles

In the following, we show the vector magnetometry without bias magnetic field using NV ensembles.

First, a magnetic field $\boldsymbol{B} = B_0(\sin\theta\cos\alpha,\ \sin\theta\sin\alpha,\ \cos\theta)$ is generated by the Helmholtz coils to simulate the magnetic field of a sample to be measured. The ODMR spectrums of NV ensembles are measured under various polarized angle θ_e of the input laser, and a two-dimensional ODMR spectrum $P_{\rm norm}(\omega, \theta_e)$ is obtained.

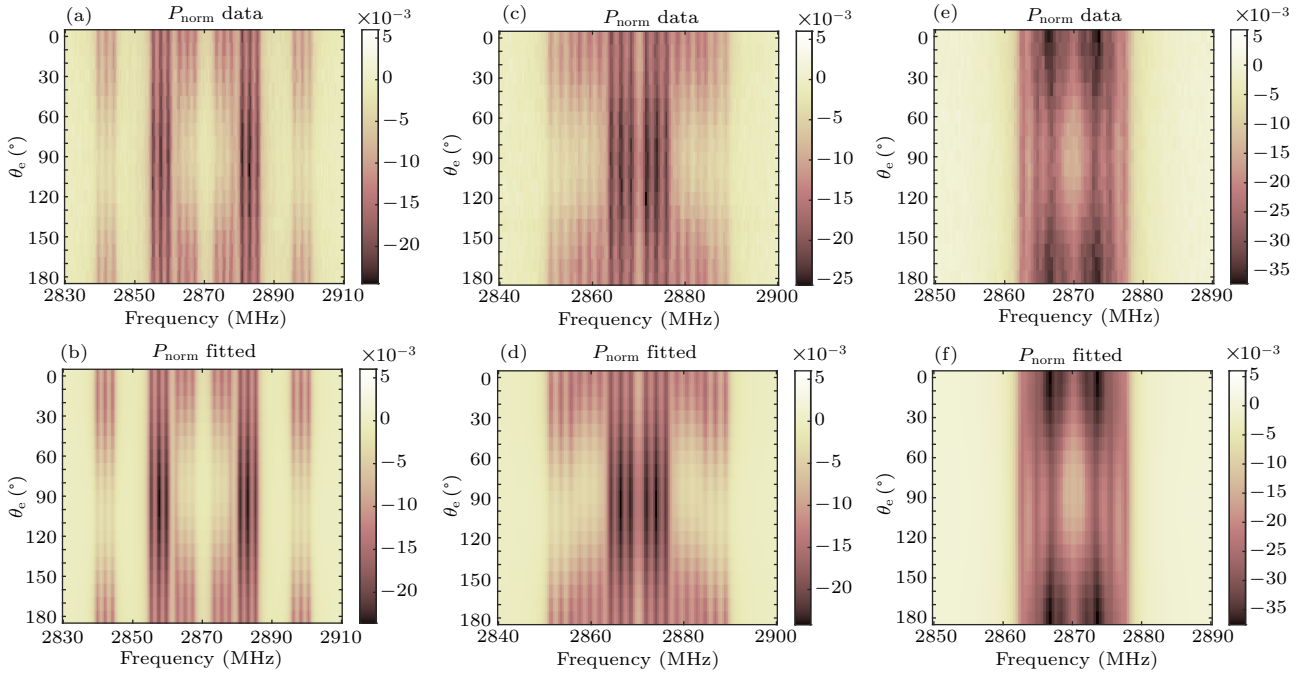


Fig. 6. Three vector magnetometry experiments in zero bias magnetic field based on NV ensembles with different magnetic field $\boldsymbol{B}$. Panels (a), (c), and (e) are measured two-dimensional ODMR spectrums $P_{\rm norm}(\omega, \theta_e)$ data. Panels (b), (d), and (f) are the corresponding calculated $P_{\rm norm}(\omega, \theta_e)$ pattern with the fitting result $\boldsymbol{B}'$ substituted in Eq. (18). The values of original field $\boldsymbol{B}$ and the reconstructed field $\boldsymbol{B}'$ are listed in Table 2.

Table 2. The detailed results of the reconstruction of the magnetic fields in Fig. 6. All the original field $\boldsymbol{B}$ and reconstructed field results $\boldsymbol{B}'$ are listed. Relative error is defined as $\eta = |\boldsymbol{B}' - \boldsymbol{B}|/|\boldsymbol{B}|$.

Exp	$\boldsymbol{B} = (B, \theta, \alpha)$	$\boldsymbol{B}' = (B', \theta', \alpha')$	$(\Delta B, \Delta\theta, \Delta\alpha)$	Relative error η
a	(10 G, 129°, 116°)	(10.156±0.007 G, 128.19°±0.08°, 115.22°±0.03°)	(0.156 G, −0.81°, −0.78°)	0.024
b	(6 G, 73°, 278°)	(6.223±0.008 G, 73.5°±0.1°, 278.47°±0.05°)	(0.223 G, 0.5°, 0.47°)	0.039
c	(2 G, 167°, 100°)	(2.146±0.008 G, 164°±1°, 92.6°±0.3°)	(0.146 G, −3°, −7.4°)	0.097

Second, the data of the two-dimensional ODMR spectrum is imported into the fitting program. With the knowledge of all the parameters determined in Table 1, the same nonlinear least-square algorithm (trust-region method) is used to fit the magnetic field vector. A selection strategy (details in the supplementary) is adopted to ensure the accuracy of the fitting result.

Then, the magnetic field $\boldsymbol{B}$ to be measured is changed and several groups of experiments are done in different $\boldsymbol{B}$. The results are shown in Fig. 6 and Table 2. When $|\boldsymbol{B}| < 20$ G and the ODMR spectrum are highly overlapped, this reconstruction method still holds high accuracy with capability of vector magnetometry. Of course, when $|\boldsymbol{B}| > 20$ G, this method is also applicable, making it a vector magnetometry method with wider dynamic range.

We gradually decreased the modulus of the magnetic field $\boldsymbol{B}$ to be measured, randomly selecting the azimuth angle α and deviation angle θ of $\boldsymbol{B}$, and reconstruct $\boldsymbol{B}$ from the data of the two-dimensional ODMR spectrum $P_{\text{norm}}(\omega, \theta_e)$ through nonlinear least-square fitting with Eq. (18). When the modulus of $\boldsymbol{B}$ is 10 G, the relative error of the reconstruction $\eta = |\boldsymbol{B}' - \boldsymbol{B}|/|\boldsymbol{B}|$ is 2.4%. When $|\boldsymbol{B}| = 6$ G and $|\boldsymbol{B}| = 2$ G, the spectrums are totally overlapped and the relative errors η increase to 3.9% and 9.7%, respectively. The experiments of $|\boldsymbol{B}| = 0.5$ G are also tested but the reconstructed results are unreliable ($\eta > 10\%$).

The minimum modulus of resolvable magnetic field $|\boldsymbol{B}_{\text{min}}|$ relates to the largest ODMR spectral linewidth of NV ensembles, Ω_{max}. We theoretically estimate that $|\boldsymbol{B}_{\text{min}}| \approx \Omega_{\text{max}}/\gamma = 0.64$ G. This is judged from the fact that when two neighboring spectral lines are too close, they will overlap and be indistinguishable. A separation of $\sim \Omega_{\text{max}}$ at least between neighboring spectral lines is necessary to realize the reconstruction. The estimation of $|\boldsymbol{B}_{\text{min}}|$ is contradictory to the experimental results that the reconstruction is unreliable when $|\boldsymbol{B}| < 2$ G.

We speculate that the extra errors in the experiments are caused by the uncertainties of the calibrated parameters in Table 1. Even though the uncertainty of each parameter is relatively small, the accumulative errors in fitting the magnetic field vector can be non-negligible since 16 parameters are related. This is supported by the simulation in Fig. 7 and Table 3.

In this simulation, the origins of the errors in reconstruction are analyzed. A $P_{\text{norm}}(\omega, \theta_e)$ spectrum (Fig. 7(a)) calculated by Eq. (18) added with the same noise level as measured in experiment is considered as the "data" imported into the reconstruction program and tested by the fitting process. Since all the parameters in Eq. (18) are controllable in simulation, the parameters in Table 1 used in reconstruction process are set to be identical with those set in calculating the "data" of the $P_{\text{norm}}(\omega, \theta_e)$ spectrum (Fig. 7(a)). So, these parameters are considered to be accurate strictly with no errors in the fitting process. The results in Fig. 7 and Table 3 show that even when $|\boldsymbol{B}|$ decreases to 0.5 G ($\boldsymbol{B} = (0.5\text{ G}, 136°, 208°)$ in spherical coordinates), the relative error η is as low as 0.4% and the reconstruction is fairly successful. This final error of fitted $\boldsymbol{B}$ originates from only the model, the fitting algorithm, and the noises added into the calculated $P_{\text{norm}}(\omega, \theta_e)$ spectrum. The numerical model itself and the fitting algorithm introduce little error in the fitting results. Thus, we infer that the extra errors in the experiment are caused by the uncertainties of the calibrated parameters.

The calibration still needs to be improved to do reconstruction of magnetic field lower than 2 G. Another apparent suggestion for improvement is to use a diamond sample of accurate $\{111\}$ facet cut ($\beta_1 = 0$ but holding $\beta_2 \neq 0$). In this circumstance, two parameters β_1 and φ_1 do not need to be calibrated and the accumulated errors to the final reconstructed field can be decreased.

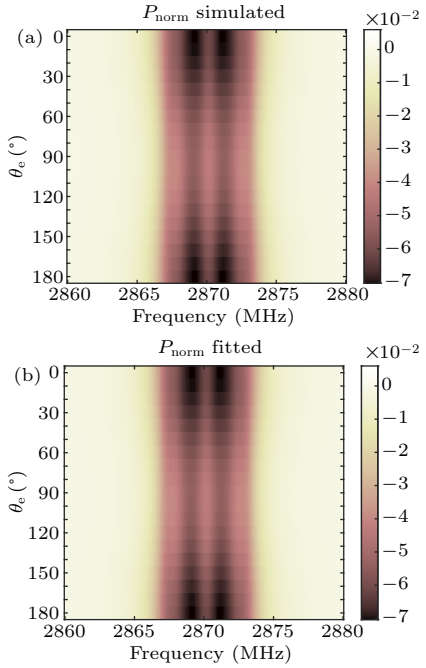


Fig. 7. A simulation to analyze the origins of the errors in reconstruction. (a) A calculated two-dimensional ODMR spectrum $P_{\text{norm}}(\omega, \theta_e)$ where $\boldsymbol{B} = (B_0, \theta, \alpha) = (0.5\text{ G}, 136°, 208°)$ using Eq. (18) by considering a RMS fluorescence contrast noise of 0.000457 according to the experimental data of Fig. 6(a). (b) The calculated two-dimensional spectrum obtained by fitting the magnetic field from (a) and substituting the fitting results into Eq. (18). The details of the fitting results are shown in Table 3.

Table 3. The detailed results of the reconstruction of the magnetic fields in Fig. 7.

Exp	$\boldsymbol{B} = (B, \theta, \alpha)$	$\boldsymbol{B}' = (B', \theta', \alpha')$	$(\Delta B, \Delta\theta, \Delta\alpha)$	Relative error η
d	(0.5 G, 136°, 208°)	(0.499±0.001 G, 136.1°±0.3°, 208.3°±0.1°)	(−0.001 G, 0.1°, 0.3°)	0.004

Nevertheless, this simulation suggests that the minimum modulus of resolvable magnetic field $|\boldsymbol{B}_{\min}|$ is theoretically down to 0.5 G using the numerical model of the two-dimensional spectrum. This shows the limited power of our reconstruction method to sense magnetic field vector in zero bias magnetic field.

6. Conclusion

We proposed a numerical model to resolve the two-dimensional ODMR spectrum measured in zero bias magnetic field using NV ensembles to reconstruct the unknown static magnetic field vector. This method overcomes the problem of overlapped spectral lines when $|\boldsymbol{B}| < 20$ G. It broadens the measurement dynamic range of magnetic field and still maintains the capacity of acquiring vector information with high accuracy. The original necessity of a bias field not less than 20 G is eliminated, making it a candidate magnetometry to be used in magnetic shield environment. This expands the application of vector magnetometry based on NV ensembles. The new magnetometry method is suitable for research about magnetic thin film materials in condensed matter physics, rock magnetism, and other materials that are sensitive to an outside magnetic field. With the future improvement of a selective circularly polarized radiation structure, the ambiguity of the plus–minus sign of reconstructed magnetic field can be eliminated and a vector magnetic field imaging method in zero bias magnetic field is available.

Acknowledgements

Project supported by the National Key R&D Program of China (Grant Nos. 2021YFB3202800 and 2023YF0718400), Chinese Academy of Sciences (Grant No. ZDZBGCH2021002), Chinese Academy of Sciences (Grant No. GJJSTD20200001), Innovation Program for Quantum Science and Technology (Grant No. 2021ZD0303204), Anhui Initiative in Quantum Information Technologies, USTC Tang Scholar, and the Fundamental Research Funds for the Central Universities.

References

[1] Goldman M L, Sipahigil A, Doherty M W, Yao N Y, Bennett S D, Markham M, Twitchen D J, Manson N B, Kubanek A and Lukin M D 2015 *Phys. Rev. Lett.* **114** 145502

[2] Balasubramanian G, Neumann P, Twitchen D, Markham M, Kolesov R, Mizuochi N, Isoya J, Achard J, Beck J, Tissler J, Jacques V, Hemmer P R, Jelezko F and Wrachtrup J 2009 *Nat. Mater.* **8** 383

[3] Bauch E, Hart C A, Schloss J M, Turner M J, Barry J F, Kehayias P, Singh S and Walsworth R L 2018 *Phys. Rev. X* **8** 031025

[4] Stanwix P L, Pham L M, Maze J R, Le Sage D, Yeung T K, Cappellaro P, Hemmer P R, Yacoby A, Lukin M D and Walsworth R L 2010 *Phys. Rev. B* **82** 201201

[5] Maertz B J, Wijnheijmer A P, Fuchs G D, Nowakowski M E and Awschalom D D 2010 *Appl. Phys. Lett.* **96** 092504

[6] Steinert S, Dolde F, Neumann P, Aird A, Naydenov B, Balasubramanian G, Jelezko F and Wrachtrup J 2010 *Rev. Sci. Instrum.* **81** 043705

[7] Wang P, Yuan Z, Huang P, Rong X, Wang M, Xu X, Duan C, Ju C, Shi F and Du J 2015 *Nat. Commun.* **6** 6631

[8] Dolde F, Fedder H, Doherty M W, Nobauer T, Rempp F, Balasubramanian G, Wolf T, Reinhard F, Hollenberg L C L, Jelezko F and Wrachtrup J 2011 *Nat. Phys.* **7** 459

[9] Cheng Z, Ye X Y, Wu J D, Yu P, Wang C J, Wang M Q, Duan C K, Wang Y, Shi F Z, Tian C L, Chen H W, Wang P F and Du J F 2023 *Phys. Rev. Applied* **19** 014057

[10] Neumann P, Jakobi I, Dolde F, Burk C, Reuter R, Waldherr G, Honert J, Wolf T, Brunner A, Shim J H, Suter D, Sumiya H, Isoya J and Wrachtrup J 2013 *Nano Lett.* **13** 2738

[11] Foy C, Zhang L, Trusheim M E, Bagnall K R, Walsh M, Wang E N and Englund D R 2020 *ACS Applied Materials & Interfaces* **12** 26525

[12] Kehayias P, Turner M J, Trubko R, Schloss J M, Hart C A, Wesson M, Glenn D R and Walsworth R L 2019 *Phys. Rev. B* **100** 174103

[13] Broadway D A, Johnson B C, Barson M S J, Lillie S E, Dontschuk N, McCloskey D J, Tsai A, Teraji T, Simpson D A, Stacey A, McCallum J C, Bradby J E, Doherty M W, Hollenberg L C L and Tetienne J P 2019 *Nano Lett.* **19** 4543

[14] Dovzhenko Y, Casola F, Schlotter S, Zhou T X, Buttner F, Walsworth R L, Beach G S D and Yacoby A 2018 *Nat. Commun.* **9** 2712

[15] van der Sar T, Casola F, Walsworth R and Yacoby A 2015 *Nat. Commun.* **6** 7886

[16] Fu R R, Weiss B P, Lima E A, Kehayias P, Araujo J F D F, Glenn D R, Gelb J, Einsle J F, Bauer A M, Harrison R J, Ali G A H and Walsworth R L 2017 *Earth and Planetary Science Letters* **458** 1

[17] Glenn D R, Fu R R, Kehayias P, Le Sage D, Lima E A, Weiss B P and Walsworth R L 2017 *Geochemistry, Geophysics, Geosystems* **18** 3254

[18] Turner M J, Langellier N, Bainbridge R, Walters D, Meesala S, Babinec T M, Kehayias P, Yacoby A, Hu E, Lončar M, Walsworth R L and Levine E V 2020 *Phys. Rev. Applied* **14** 014097

[19] Fleig T, Frontera P and Ieee 2018 *IEEE/ION Position, Location and Navigation Symposium (PLANS)*, 2018 Apr 23–26, Monterey, CA, pp. 1107–1112

[20] Dunlop D J and Özdemir Ö 1997 *Rock Magnetism: Fundamentals and Frontiers* (Cambridge: Cambridge University Press)

[21] Lenz T, Wickenbrock A, Jelezko F, Balasubramanian G and Budker D 2021 *Quantum Science and Technology* **6** 034006

[22] Zheng H, Xu J, Iwata G Z, Lenz T, Michl J, Yavkin B, Nakamura K, Sumiya H, Ohshima T, Isoya J, Wrachtrup J, Wickenbrock A and Budker D 2019 *Phys. Rev. Applied* **11** 064068

[23] Münzhuber F, Bayer F, Marković V, Brehm J, Kleinlein J, Molenkamp L W and Kiessling T 2020 *Phys. Rev. Applied* **14** 014055

[24] Barry J F, Schloss J M, Bauch E, Turner M J, Hart C A, Pham L M and Walsworth R L 2020 *Rev. Mod. Phys.* **92** 015004

[25] Alegre T P M, Santori C, Medeiros-Ribeiro G and Beausoleil R G 2007 *Phys. Rev. B* **76** 165205

[26] Lagarias J C, Reeds J A, Wright M H and Wright P E 1998 *SIAM Journal on Optimization* **9** 112

[27] Reuschel P, Agio M and Flatae A M 2022 *Advanced Quantum Technologies* **5** 2200077